Current-controlled unidirectional edge-meron motion

Xiangjun Xing,[1,2] Philip W. T. Pong,[1] and Yan Zhou[3,a)]
[1]*Department of Electrical and Electronic Engineering, The University of Hong Kong, Hong Kong, China*
[2]*School of Physics and Optoelectronic Engineering, Guangdong University of Technology, Guangzhou 510006, China*
[3]*School of Science and Engineering, The Chinese University of Hong Kong, Shenzhen 518172, China*

(Received 20 September 2016; accepted 10 November 2016; published online 29 November 2016)

In order to address many of the challenges and bottlenecks currently experienced by traditional charge-based technologies, various alternatives are being actively explored to provide potential solutions of device miniaturization and scaling in the post-Moore's-law era. Amongst these alternatives, spintronic physics and devices have recently attracted rapidly increasing interest by exploiting the additional degree of electrons-spin. For example, magnetic domain-wall racetrack-memory and logic devices have been realized via manipulating domain-wall motion. As compared to domain-wall-based devices, magnetic skyrmions have the advantages of ultrasmall size (typically 5–100 nm in diameter), facile current-driven motion, topological stability, and peculiar emergent electrodynamics, promising for next-generation electronics applications in the post-Moore's-law regime. Here, a magnetic meron device, which behaves similarly to a PN-junction diode, is demonstrated for the first time, by tailoring the current-controlled unidirectional motion of edge-merons (i.e., fractional skyrmions) in a nanotrack with interfacial Dzyaloshinskii-Moriya interaction. The working principles of the meron device, theoretically predicted from the Thiele equation for topological magnetic objects, are further verified using micromagnetic simulations. The present study has revealed the topology-independent transport property of different magnetic objects and is expected to open the vista toward integrated composite circuitry (with unified data storage and processing) based on a single magnetic chip, as the meron device can be used, either as a building block to develop complex logic components or as a signal controller to interconnect skyrmion, domain-wall, and even spin-wave devices. *Published by AIP Publishing*. [http://dx.doi.org/10.1063/1.4968574]

I. INTRODUCTION

Magnetic skyrmions are topologically stable spin configuration with an unit skyrmion number (Q) that can exist in non-centrosymmetric bulk magnets[1,2] and ultrathin magnetic multilayer films lacking inversion symmetry,[3] where asymmetric Dzyaloshinskii-Moriya interaction (DMI)[4–7] mediated by certain atoms with a strong spin-orbit coupling tends to twist the adjacent spins. Once a current is applied, the quantized topological charge can help a skyrmion to avoid pinning centers[8–10] but causes accompanying transverse displacement during its drift motion along a transmission channel, giving rise to the so-called skyrmion Hall effect.[8,9,11,12] The skyrmion Hall effect can be eliminated by using a bilayer composite structure.[13] At sufficiently large current densities where the Magnus force overcomes the boundary's repulsion force, a skyrmion will be pushed to touch the lateral boundary of a transmission track, forming a fractional skyrmion termed edge-meron.[14] Then, the inward directed repulsion force acting on the skyrmion converts into an outward directed attraction force on the edge-meron. In terms of string geometry,[15] an edge-meron is enclosed by a curved open string and a boundary of a transmission channel, and therefore, it can be deemed as an intermediate spin texture between a skyrmion with $Q = 1$ and a domain-wall pair with $Q = 0$. Intrinsically, edge-merons are highly unstable instantons[16] because of the loss of topological protection. If no current is applied, an edge-meron will decay rapidly. According to the Thiele equation,[17] an edge-meron will experience a Magnus force[18–20] when a current is employed, since the skyrmion number for an edge-meron is still finite despite being smaller than 1.[14] The direction of the Magnus force depends on that of the in-plane current along a track.[8–10] Thus, the Magnus force can be tuned to favor or react against the boundary's attraction force by changing the current direction.

By micromagnetic simulations, we address the current-driven dynamics of magnetic edge-merons in a nanotrack made of an ultrathin multilayer film exhibiting interfacial DMI.[6,7] We find that, for a certain current direction, the Magnus force on the edge-meron can indeed counteract the boundary's attraction force, resulting in the edge-meron's dynamical stabilization in the transverse direction and its steady flow along the boundary at a velocity proportional to the current density. When the current direction is reversed, the edge-meron is expelled from the boundary. These findings are in accordance with the prediction of the Thiele equation.[18,19] Remarkably, the mobility (i.e., the velocity over the current density) for the edge-merons and skyrmions appears to be irrelevant to the topological numbers of these magnetic objects as well as the material parameters, even though the topological charge of an edge-meron changes with the applied current density.

The fact that the nonreciprocal motion of an edge-meron along the boundary is dependent on the current direction

a)E-mail: zhouyan@cuhk.edu.cn

allows for a current-controlled meron device, which shall be patterned into a lateral-junction-type nanotrack with the central part serving as the modulation unit and the two side arms as the output element. The in-plane current is chosen as the control signal (as what the bias voltage behaves in conventional PN-junction diode[21]), and the inductive voltage on the detection coil traversed by a moving domain wall (converted from an edge-meron stabilized in the central track) is encoded into the output signal. Numerical simulations demonstrate that the proposed device can operate over a broad range of the parameter space and even at room temperature. Meron-based signal processing together with the well-known domain-wall logic[22] and racetrack-memory[23] technologies should lay the foundation for magnetic computers[24,25] beyond the von Neumann architecture with strictly separated logic and memory.

II. MATERIALS AND METHODS

A. Theoretical prediction based on the Thiele equation

The Landau-Lifshitz-Gilbert equation is a well-established general-purpose tool in describing spin dynamics of any continuous ferromagnetic system.[8–10,13,15,18,19,24,26,27] From this general equation of motion of magnetization, the so-called Thiele equation can be derived to describe the motion of center of mass of a rigid spin texture[8,10,19]

$$\mathbf{G}\times(\mathbf{v}^{\mathrm{s}}-\mathbf{v}^{\mathrm{d}})-\nabla V+\mathcal{D}(\beta\mathbf{v}^{\mathrm{s}}-\alpha\mathbf{v}^{\mathrm{d}})=0, \tag{1}$$

representing the balance of the Magnus, confining, and viscous forces, where the gyrocoupling vector $\mathbf{G}=G\hat{\mathrm{e}}_z$ with $\hat{\mathrm{e}}_z$ being the unit vector along the vertical z axis, V is the confining potential due to boundaries, impurities, and/or magnetic fields, and $\mathcal{D}=\begin{pmatrix}\mathcal{D}_{xx} & \mathcal{D}_{xy}\\ \mathcal{D}_{yx} & \mathcal{D}_{yy}\end{pmatrix}=\begin{pmatrix}\mathcal{D} & 0\\ 0 & \mathcal{D}\end{pmatrix}$ is a dissipation tensor. α is the Gilbert damping parameter, β is the relative strength of the nonadiabatic and adiabatic spin torques in the Zhang-Li form associated with an in-plane current,[28,29] $\mathbf{v}^{\mathrm{d}}$ is the drift velocity of the spin texture, and $\mathbf{v}^{\mathrm{s}}$ is the velocity of conduction electrons that is equal to the electron current density $\mathbf{j}=-J\hat{\mathrm{e}}_x$ multiplied by a prefactor $\gamma\hbar P/(2\mu_0 eM_s)$, where J is the magnitude of electric current density, $\hat{\mathrm{e}}_x$ the unit vector in the x direction, γ the gyromagnetic ratio, μ_0 the vacuum permeability, $\hbar$ the reduced Planck constant, P the spin polarization of flowing electrons in the nanotrack, e the elementary charge, and M_{s} the saturation magnetization.

The gyroconstant G is proportional to Q,[8,9] which is 1 for a skyrmion and 0 for a domain wall. Consequently, the Magnus force $\mathbf{F}_{\mathrm{g}}=\mathbf{G}\times(\mathbf{v}^{\mathrm{s}}-\mathbf{v}^{\mathrm{d}})$ will act on a moving skyrmion if $\mathbf{v}^{\mathrm{d}}\neq\mathbf{v}^{\mathrm{s}}$, and it is always absent for domain walls. When a skyrmion moves along a nanotrack, it experiences bilateral confining potential; therefore, once the skyrmion, under the Magnus force, departs from the center of the track to approach one of the two borders, the confining force $\mathbf{F}_{\mathrm{p}}=-\nabla V$ will emerge from that border as an opposing force.[8,9] Finally, under appropriate driving current densities, the skyrmion will remain stabilized transversally and drift steadily along the nanotrack,[8,9] that is, the Magnus force can always be compensated by the confining force from either boundary, irrespective of the skyrmion's drift direction.

Provided that an edge-meron can preserve a rigid structure, its current-driven motion should satisfy the above Thiele equation. An edge-meron lies at a specific border; thus, the force $\mathbf{F}_{\mathrm{p}}$ from that border has a definite direction. As a result, if the force $\mathbf{F}_{\mathrm{p}}$ is oppositely directed with respective to $\mathbf{F}_{\mathrm{g}}$ for a certain current direction, they will point in the same direction when the applied current is reversed (as illustrated in Fig. 1). Equation (1) requires that the topological charge Q is nonzero and $\mathbf{v}^{\mathrm{d}}\neq\mathbf{v}^{\mathrm{s}}$ in order for a finite $\mathbf{F}_{\mathrm{g}}$ on the edge-meron to occur. By applying an in-plane current along the track (i.e., the x axis) and assuming that, under the given current density, the edge-meron reaches steady-state motion, one gets $v_y^s=0$, $v_y^d=0$, $\mathcal{D}(\beta\mathbf{v}^{\mathrm{s}}-\alpha\mathbf{v}^{\mathrm{d}})=0$, and $\mathbf{F}_{\mathrm{g}}+\mathbf{F}_{\mathrm{p}}=0$. After some algebra, one obtains[9]

$$v_x^{\mathrm{d}}=(\beta/\alpha)v_x^{\mathrm{s}}, \tag{2}$$

and

$$F_{\mathrm{g}}=(1-\beta/\alpha)Gv_x^{\mathrm{s}}=-F_{\mathrm{p}}, \tag{3}$$

which requires $1-\beta/\alpha\neq 0$, $G\neq 0$, and $v_x^s\neq 0$ (i.e., $\beta\neq\alpha$, $Q\neq 0$, and $J\neq 0$) for an edge-meron to enter into steady drift motion. Otherwise, the edge-meron will destabilize and annihilate finally. It is worthy noting that the amplitude and direction of J—an adjustable parameter—can be conveniently tuned to tailor the alignment of forces. As a next step, we resort to micromagnetic simulations to test the assumptions and theoretical predictions made herein.

B. Numerical verification by micromagnetic simulations

The nanotracks, used as transmission channel for magnetic merons, are patterned from an ultrathin multilayer film with asymmetric interfaces to engender an interfacial DMI.[6,7] In what follows, we will demonstrate, first, the fundamental principle of nonreciprocal edge-meron transport along the boundary channel under in-plane currents. Here, we use a magnetic nanotrack 1200 nm in length and 60 nm in width, in which an edge-meron is preset and then moved by an in-plane current (Figs. 2–4 and Figs. S1 and S2 in the supplementary material). Current-driven skyrmion motion in the same nanotrack is also examined for comparison.[8,9] Subsequently, we will check the influence of edge irregularity on meron motion. For this, a triangular notch[8,30] with variable depth is included into the border of the nanotrack to mimic the boundary defect[31] (Fig. 5). Finally, we will demonstrate how a meron device works by virtue of the current-modulated unidirectional motion of edge-merons. To this end, a planar-junction-type structure composed of nanotracks with different widths[15,32] is adopted (Fig. 6 and Figs. S3 and S4 in the supplementary material). The thickness of the tracks for all simulations is 1 nm.

Micromagnetic simulations based on MuMax3[33] were carried out to study the injection of an edge meron under a perpendicular current and to trace the dynamics of meron motion under an in-plane current. For all computations, the interfacial DMI[34] was added into the conventional Landau-Lifshitz-Gilbert (LLG) equation,[35,36] for those computations examining spin dynamics triggered by the out-of-plane

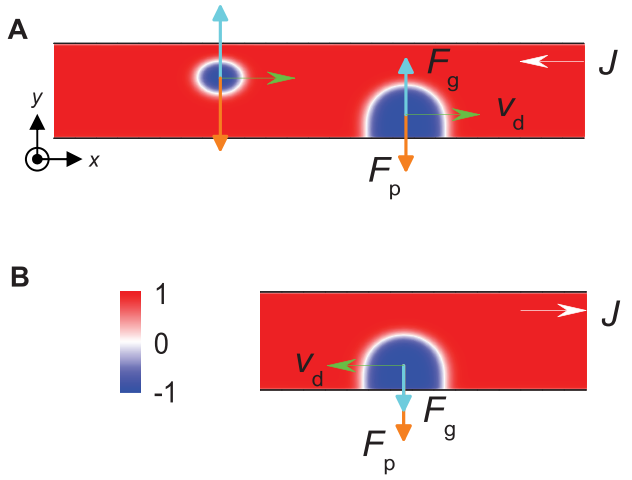

FIG. 1. Layout showing the relationship between transverse forces ($\mathbf{F}_g$ and $\mathbf{F}_p$) and longitudinal drift velocity ($\mathbf{v}^d = v_x^d \hat{\mathbf{e}}_x$) for an edge-meron. The drift velocity of the meron depends on the driving current density (note that $\mathbf{j} = -J\hat{\mathbf{e}}_x$). (a) For leftward injected electric currents, the Magnus force ($\mathbf{F}_g$) reacts against the boundary's attraction force ($\mathbf{F}_p$) and thus can result in steady-state meron motion for J in a certain range. The force balance for a skyrmion, with a positive velocity, is shown for comparison. (b) For rightward flowing electric currents, the Magnus force then favors the attraction force, repelling the edge-meron out of the track.

current, the Slonczewski spin torque[37] was included as well, and for those tackling spin dynamics stimulated by the in-plane current, the Zhang-Li spin torque[28,29] was incorporated additionally. For finite-temperature simulations, the random thermal field of the Brown form[33] was included into the effective magnetic field (the results are shown in Fig. S4). The material parameters typical of Pt/Co multilayer systems with perpendicular magnetic anisotropy were employed in simulations:[8,15] $M_s = 580$ kA m^{-1}, the exchange stiffness $A = 15$ pJ m^{-1}, $P = 0.4$, and $\alpha = 0.3$ ($\alpha = 0.05$[9,38] and 0.01[39,40] were also examined in simulations to see the influence of damping constant; see Figs. 4 and S2). According to Eq. (3), $\beta/\alpha = 1$ shall lead to zero Magnus force and thus destabilization of the edge-meron motion; therefore, the other two representative cases of $\beta/\alpha = 2$ and 0.5 were considered in simulations. A series of K_u (perpendicular magnetocrystalline anisotropy) and D (the DMI strength) combinations were examined in computations to ensure that the obtained results would be valid for a variety of samples[8,15] (Fig. 3 and Figs. S2 and S3 in the supplementary material). The results presented in the figures throughout the paper correspond to $K_u = 0.8$ MJ m^{-3} (the effective uniaxial anisotropy $K_{eff} = 0.6$ MJ m^{-3} as given by $K_{eff} = K_u - (1/2)\mu_0 M_s^2$) and $D = 3.5$ mJ m^{-2} unless specified otherwise. The computational volume was divided into regular meshes of $1 \times 1 \times 1$ nm^3 regardless of the sample size. We did not impose any additional boundary condition on the system in our simulations. Instead, we used the open boundary condition, which should reflect the realistic circumstance (i.e., the properties of the real boundary).

III. RESULTS

A. Unidirectional motion of edge-merons

The rigidity of the meron's spin configuration is well maintained during its motion along a track without including imperfections, as clearly seen from Figs. 2(a) and 2(c), where the edge-meron moves smoothly showing a stable shape and structure especially after the establishment of steady drift motion characterized by unvaried m_z and Q with time after 1.5 ns [Figs. 2(b) and 2(d)]. The steady drift of the edge-meron along the track [Figs. 2(a) and 2(c)] implies that the Magnus force occurs to the meron and cancels out the drag force of the boundary. Without the current-induced Magnus force, the meron will be pushed away from the track soon (Fig. S1(c)), where $\mathbf{v}^d = \mathbf{v}^s$ (resulting from $\alpha = \beta$) permits no gyrotropic force, as expected from Eq. (3). The occurrence of the Magnus force to the meron suggests that the edge-meron has nonzero topological charge, as is confirmed by the numerical values of Q [Figs. 2(b) and 2(d)] directly calculated from the simulated spin configuration according to $Q = (1/4\pi)\int \mathbf{m} \cdot (\partial_x \mathbf{m} \times \partial_y \mathbf{m}) \mathrm{d}x\mathrm{d}y$.[15]

By reversing the current direction in Fig. 2(a) with the other parameters unaltered, we arrive at the results in Figs. 2(e) and 2(f) displaying that the edge-meron decays quickly. Apparently, the Magnus force and the attraction force from the boundary combine into an outward net force, which drags the meron. That is to say, the Magnus force can be reversed by simply reversing the current direction verifying the theoretical prediction [Eq. (3)] of the Thiele equation. The orientation of the Magnus force determines the dynamics of the edge-meron, as seen from comparing Figs. 2(a) and 2(b) and Figs. 2(e) and 2(f). In a word, when the Magnus force balances the boundary's attraction force in the transverse direction, the meron drifts steadily along the boundary channel; when the Magnus force is opposite to the boundary's force, the meron is annihilated after injection at a timescale of hundreds of picoseconds [Figs. 2(e) and 2(f) and S1(a)–S1(c)]. In this way, unidirectional transmission of meron carriers is realized.

In Fig. 2(c), $1 - \beta/\alpha = 0.5$ has a sign opposite to $1 - \beta/\alpha = -1$ in Fig. 2(a), and meanwhile the current directions are also opposite. Considering that the boundary's force is always outward directed, the directions of the Magnus forces in Figs. 2(a) and 2(c) must be identical and inward directed to keep the steady-state motion. This agrees with the anticipation of Eq. (3). At this point, Eq. (3) (the dependencies of $\mathbf{F}_g$ on β/α, Q, and J) has been thoroughly substantiated by simulation results.

According to Eq. (2), the velocity of a spin texture has nothing to do with its topological charge, which is revealed in Fig. 2(c) where a skyrmion with $Q \sim 1$ and an edge-meron with $Q \sim 0.5$ move synchronously along the track, just as if they were bound together despite no interaction between them. This will be further validated by additional simulation results in Fig. 4 indicating the topological charge of an edge-meron changing with the driving current density. The good agreement between the simulated and analytical results suggests that the meron dynamics under in-plane currents can be well captured by Eq. (1)—the massless Thiele equation—at least for perfect tracks without defects.

To reach the steady-state motion, the drag force from the boundary must be rigorously offset by the Magnus force. The boundary's force sensed by the edge-meron is determined by the potential landscape of the track,[8,9] which is

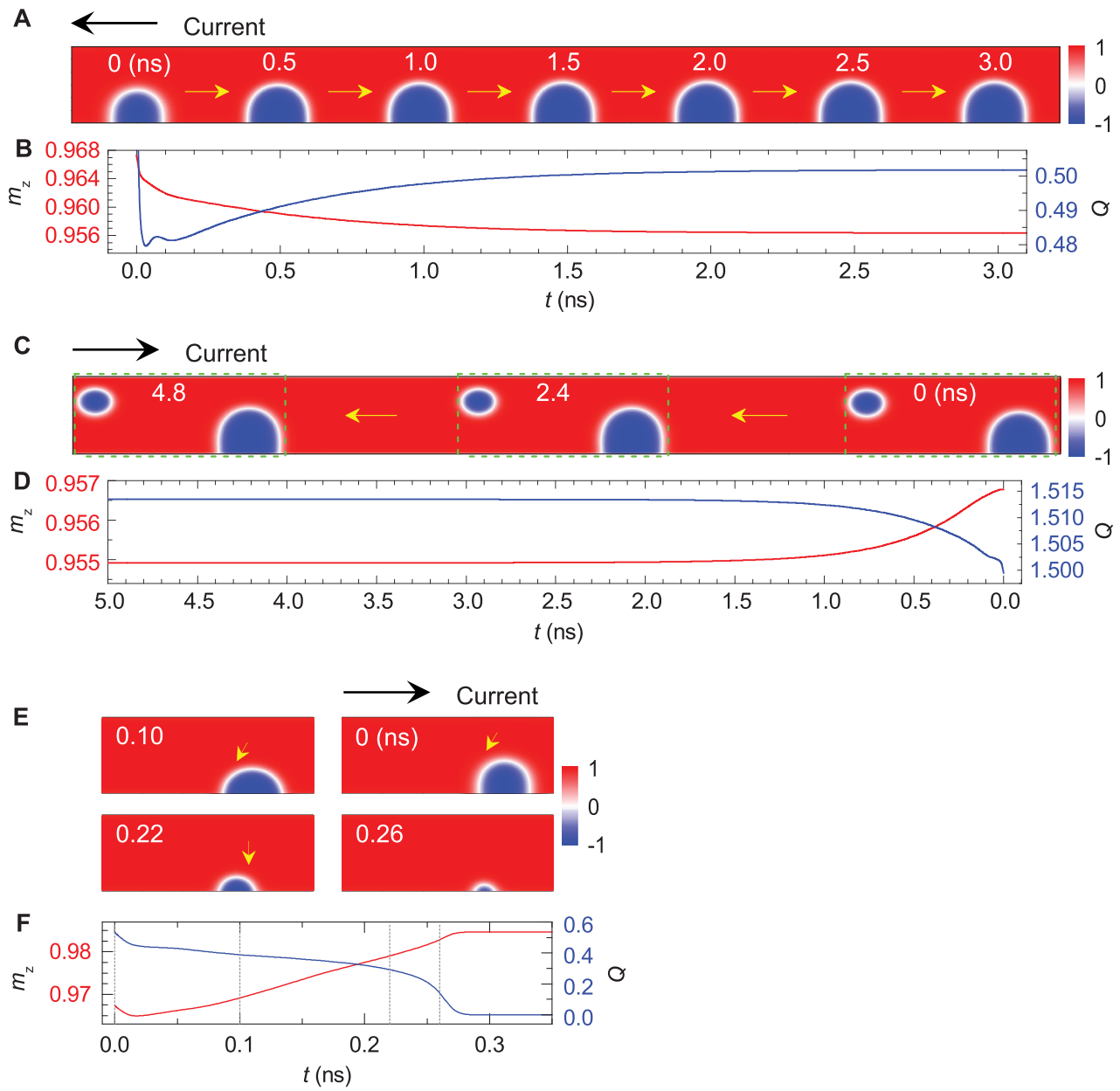

FIG. 2. Unidirectional motion of edge-merons. (a)–(d) Steady-state drift motion of edge-merons under an in-plane current. (a) Snapshots of an edge-meron at indicated times. (c) Snapshots of an edge-meron as well as a skyrmion at indicated times. (b) and (d) The vertical component of normalized magnetization averaged over the entire volume of the nanotrack, m_z, and the topological charge, Q, as a function of the current action time, t, corresponding to (a) and (c), respectively. The track is 60 nm wide and 1 nm thick. $\alpha = 0.3$. In (a) and (b), β is assumed to be 2α, namely, 0.6; the electric current is leftward injected as marked by the arrow and $J = +3.0 \times 10^{12}$ A m^{-2}. In (c) and (d), β is set to be 0.5α, namely, 0.15; the applied electric current flows rightward as denoted by the arrow and $J = -5.0 \times 10^{12}$ A m^{-2}. From $F_g = (1 - \beta/\alpha)Gv_x^s \propto (\beta/\alpha - 1)J$, it is clear that, for β equal to twice and half of α, $(1 - \beta/\alpha)$ changes sign. Hence, the current directions must be reversed to maintain the fixed direction of the Magnus forces in (a) and (c). Moreover, the rigidity of the edge-meron is preserved in the motion process. The steady state is established a few nanoseconds after the application of the current, as revealed by the plateaus in the $m_z(t)$ and $Q(t)$ curves. (e) and (f) Destabilization and annihilation of an edge-meron under an in-plane current. (e) Snapshots of an edge-meron at indicated times. (f) m_z and Q versus t. Note that, here, all parameters in (e) and (f) are the same as in (a) and (b) except for the current direction. The current flows in the direction such that the Magnus force assists the drag force of the boundary. Under the joint forces, the edge-meron shrinks in size and loses the topological charge and finally is annihilated.

related to the material parameters and the shape, size, and topological charge of the meron. The topological charge of the edge-meron exhibits dependency on the driving current density. It is impossible to derive an explicit expression for $V = V[K_u, D, Q(K_u, D, J)]$ and thus for $\mathbf{F}_p = -\nabla V$. In turn, the current-density window guaranteeing steady-state meron motion cannot be analytically extracted, and numerical simulations become a proper tool to address the issue. We examine the current-driven motion of an edge-meron in the nanotrack, with K_u varying from 0.4 to 1.2 MJ m^{-3} and D varying from 2.0 to 4.5 mJ m^{-2}, which covers the range of the most technological relevance[8,15,24,27,39,41] and beyond which a regular skyrmion is not allowed to exist in the track in the remnant state [single-domain configuration for lower (K_u, D);[8] elongated-skyrmion or multi-domain configuration for higher (K_u, D)].[8,15] The results are presented in Fig. 3 as

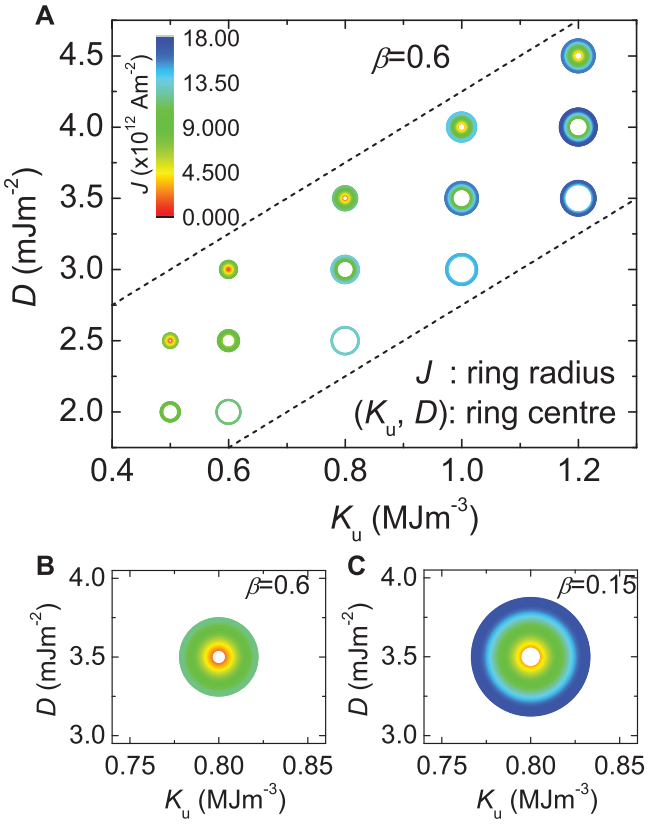

FIG. 3. Phase diagram for transverse stabilization and longitudinal steady motion of the edge-meron subject to in-plane currents. $\alpha = 0.3$. In (a), $\beta = 2\alpha$; each ring is centered at (K_u, D) with the inner and outer radii representing the lower and upper critical current densities; inside each ring, the steady-state meron motion is attainable. Apart from the radii, the colored peripheries in each ring also code the current densities. (b) and (c) The stabilization rings of an edge meron for different β/α values (all other parameters are kept the same).

a phase diagram. The colored interior of the ring (named stabilization ring here) centered at each (K_u, D) stands for the range of the current densities, under which the steady meron motion can be established. The inner area surrounded by the colored ring groups such current densities, at which the Magnus force is not large enough to compensate the boundary's force so that the meron is expelled from the track, whereas for the region outside each ring, the current density deforms an edge-meron into a domain-wall pair by inducing a much stronger Magnus force than the oppositely directed force from the boundaries.

The stabilization rings are not identical for various material parameters. For a given K_u with $\alpha = 0.3$ and $\beta = 2\alpha$, the higher the D value, the larger is the outer radius of the ring and the wider is the ring (Fig. 3(a)). At a given (K_u, D), the stabilization ring for (α, β) = (0.3, 0.5α) is wider and bigger than for (α, β) = (0.3, 2α) [Figs. 3(b) and 3(c)]. The difference in the stabilization rings reflects the complex dependences of the Magnus and boundary's forces upon the material properties. Specifically, the two forces are directly associated with the material parameters as well as the geometrical and/or topological characteristics (size, shape, topological charge, etc.) of an edge-meron, as revealed in Eq. (3). The geometry and topology of a meron are also dependent on material properties. Associating the above considerations with Eq. (3), one can get $J_s \propto -\nabla V[K_u, D, Q(K_u, D, J_s)]/Q(K_u, D, J_s)$, where J_s are the current densities allowing steady meron motion to be established when other material parameters are given. The above implicit function of J_s reveals the difficulty in analytically deriving the stabilization phase diagram and the dependence of the stabilization rings on material parameters.

Figure 4(a) shows the simulated velocity (v_x^d) versus current density (J) for steadily moving edge-merons in nanotracks with varied K_u, D, α, and β values. Clearly, the drift velocities of edge-merons are linearly proportional to the driving current densities,[8,9] which is consistent with the expectation of Eq. (2). Moreover, defining the mobility of an edge-meron as the velocity divided by the driving current density, i.e., v_x^d/J, one can see that the mobility is independent of K_u, D (material parameters), and Q (topology parameter) as long as the current density is within the corresponding stabilization ring (Fig. 3) although the topological charge Q changes with the current density J [Figs. 4(b)–4(g)]. Note that, for the relevant current densities, the Q value of an edge-meron is in the range of 0.4–0.65, which is not far from 0.5.[14] Once Q becomes too large or too small, the force balance on the meron will be broken immediately [recall that, the Magnus force $F_g \propto J \times Q(J)$], and the meron will in turn collapse into a domain-wall pair[15] (Fig. S1(d)) or disappear [Figs. 2(e) and 2(f) and S1(a)–S1(c)]. Intriguingly, it appears that the skyrmions and edge-merons have the same mobility, when identical α and β values are assumed in simulations, which evidences that the mobility of a spin texture in a given track is not affected by its topological charge, if the structural rigidity can be well maintained during its motion. The observation that the mobility is independent of K_u, D, and Q is in line with Eq. (2), where such parameters are absent and not implicitly involved as well.

According to Eq. (2), the meron mobility $\mu \equiv v_x^d/J = [\gamma\hbar P/(2\mu_0 e M_s)]\cdot(\beta/\alpha)$. Substituting the values of all constants and some parameters into the above formula, one gets $\mu = (0.400 \times 10^{-10}\beta/\alpha)$ m^3 A^{-1} s^{-1}. Thus, the theoretical mobility values are 0.800×10^{-10} m^3 A^{-1} s^{-1} for $\beta = 2\alpha$ and 0.200×10^{-10} m^3 A^{-1} s^{-1} for $\beta = 0.5\alpha$. From Fig. 4(a), one finds that, at $\alpha = 0.3$, the simulated mobility values are 0.583×10^{-10} m^3 A^{-1} s^{-1} for $\beta = 2\alpha$ and 0.194×10^{-10} m^3 A^{-1} s^{-1} for $\beta = 0.5\alpha$; whereas at $\alpha = 0.01$, the values are 0.583×10^{-10} m^3 A^{-1} s^{-1} for $\beta = 2\alpha$ and 0.381×10^{-10} m^3 A^{-1} s^{-1} for $\beta = 0.5\alpha$. The clear dependency of the mobility upon the damping parameter seen in simulation results is missing from the theoretical prediction. The slight discrepancies between the theory and simulations might be ascribed to the incompleteness of the massless Thiele equation within the rigid-body picture,[8,10,19,20] which neglects the structural deformation of a spin texture and the relaxation of the internal spins that strongly rely on the damping properties of materials.

Additional simulations verify that steady-state edge-meron motion can also exist in a B20-type nanotrack that has a bulk-type DMI; see Fig. S5 in the supplementary material. In fact, an edge-meron has been clearly demonstrated in Fig. 3(c) of Ref. 9, where a rectangular notch was cleverly designed to favor the nucleation of a meron that converts to a skyrmion later.

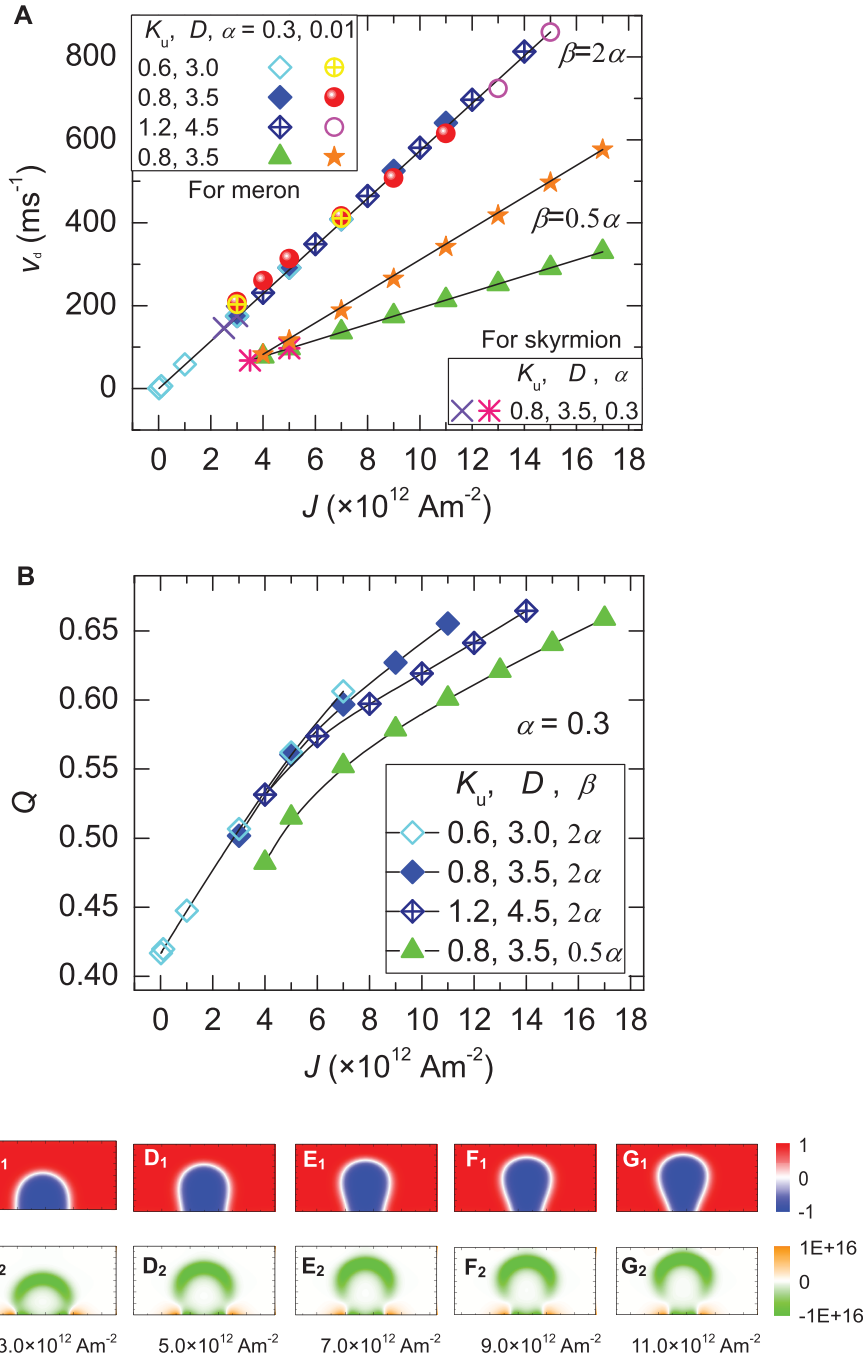

FIG. 4. Mobility of edge-merons in steady drift motion. (a) Drift velocity and (b) topological charge as a function of the current density. (c_1)–(g_1) The contours of spin configuration and (c_2)–(g_2) topological-charge density of the edge-meron under specified current densities. In (a), $\beta = 2\alpha$ and 0.5α, with $\alpha = 0.3$ and 0.01, are considered for the edge-meron, and the skyrmion motion is checked for $\beta = 2\alpha$ and 0.5α with $\alpha = 0.3$ for comparison. In (b), $\beta = 2\alpha$ and 0.5α are considered for the edge-meron only with $\alpha = 0.3$. In both (a) and (b), several (K_u, D) combinations are taken into account to see the effect of the parameter variation. In (c)–(g), $K_u = 0.8$ MJ m^{-3}, $D = 3.5$ mJ m^{-2}, $\alpha = 0.3$, and $\beta = 2\alpha$. The results in (a) suggest that the edge-merons and skyrmions have the same mobility, exhibiting no dependency on the material parameters K_u and D and the topological charge Q, which is in qualitative agreement with the theoretical result [Eq. (2)].

B. Effect of boundary roughness

In deriving the theoretical velocity and force equations, we assumed an ideal nanotrack without including any impurity or edge roughness. However, experimentally, a nanotrack prepared even by the state-of-the-art microfabrication techniques cannot avoid defects such as boundary irregularity, which affects the motion of spin textures in the track.[31] As argued above, an edge-meron is an intermediate entity between a skyrmion and a domain-wall pair. It should behave like a skyrmion in the interior and like a domain-wall pair on the border line of a track. To clarify how boundary defect influences the motional dynamics of an edge-meron under an electric current, we introduced a triangular notch[8,30] into the border of a nanotrack in simulations (inset of Fig. 5(a)). We found that the behavior of a meron in passing through the notch depends on the depth of the notch and the current density[8] [compare Figs. 5(a) and 5(b)]. For instance, at a given current density $J = +4.0 \times 10^{12}$ A m^{-2}, the meron can pass through a notch 3 nm in depth (5% of the track width) but cannot pass through a notch 6 nm in depth. If the current density is increased to $J = +6.0 \times 10^{12}$ A m^{-2}, the meron can overcome all the notches of 3, 6, and 12 nm in depth and return to the original trajectory.

As shown in Fig. 5(a), during the meron moving toward the right end, the front wall meets the notch and then detaches, and a moment later the far wall touches the notch but is tightly pinned, instead. The reason why the front wall can escape from the notch is that it senses the joint forces of the current and the far wall. The current exerts a viscous

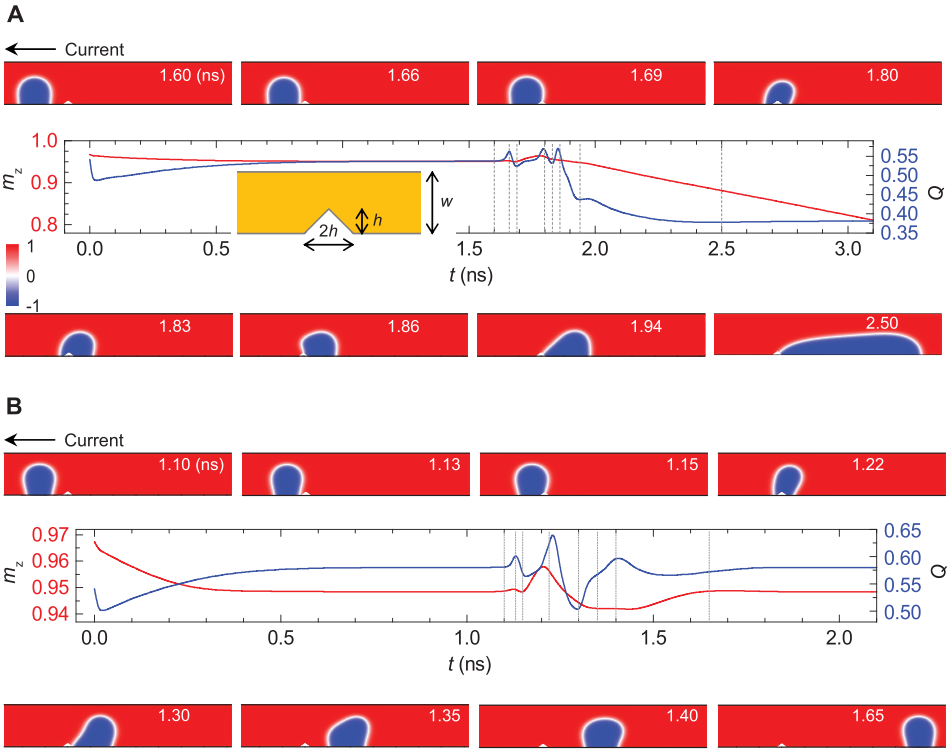

FIG. 5. Current-driven dynamics of an edge-meron in a notched nanotrack. The triangular notch [inset in (a)] models boundary roughness in real samples. Here, the depth of the notch is 10% of the width of the track, namely, $h = 0.1w$. $\alpha = 0.3$ and $\beta = 2\alpha$. In (a) and (b), the current density is $J = +4.0 \times 10^{12}$ A m^{-2} and $+6.0 \times 10^{12}$ A m^{-2}, respectively. Specified in each subpanel is the action time of the electric current. Each central panel displays m_z and Q against the current action time.

force via spin transfer; the far wall imposes a repulsive force through exchange interaction.[42] By contrast, the far wall only experiences the viscous force from the current, since the front wall has been driven away from the far wall and thus cannot offer a force (even though the front wall is close to the far wall, it cannot help the latter to depin from the notch, because its repulsive force counteracts the viscous force of the current). By pushing the front wall forward, the current elongates the meron to become into a strip domain.[15] However, the picture is different for the meron under a higher current density, as shown in Fig. 5(b), where the viscous force from the current is so large that both the front and far walls can easily escape from the notch.

C. On symmetry breaking

Figures 2 and 3 and S1 and S2 contain solid evidence for supporting the prediction (based on the Thiele equation) that the motions of edge-merons under in-plane currents are nonreciprocal over a wide range in the space of material parameters K_u, D, α, and β. Intrinsically, the unidirectionality in the meron motion should stem from the breaking in the mirror symmetry of the potential landscape [viz., $V(-y) \neq V(y)$] of the nanotrack, where the spin texture is attached to one of the two symmetric lateral boundaries. Such a potential environment makes the boundary's confining force on a meron be locked into a specific orientation and be unable to balance the Magnus force for one of the two current directions, leading finally to the current-controlled unidirectional motion of edge-merons. The nonreciprocal meron motion benefiting from the special characteristics of "edge states" resembles the edge-localized propagation of the Damon-Eshbach spin waves in a 1-dimensional magnetic waveguide.[32,43,44] Spin-wave edge channels formed by the potential wells (i.e., minimums in the internal field) near the lateral boundaries of a waveguide are induced by the boundary magnetic charges,[45,46] which can be created only if the translational symmetry of the waveguide is broken in its width direction. The occurrence of the spin-wave edge states by introducing spatially separated edge channels that accompany the center channels enables spin-wave confluence and beating in a single waveguide,[47] which might find application in multichannel information transmission and processing as well as nanometer-scale frequency deconvolution of microwave signals.[43]

D. Meron-based device

We propose a magnetic meron device (Fig. 6(a)), the key element of which is a lateral junction consisting of a wide track and two narrow arms. An edge-meron is injected into the wide track by using the Slonczewski spin torque of a perpendicular current, which is applied to a local area covered by a point-contact spin valve.[8,48] To manipulate the meron, an in-plane current will be fed into the junction through a control unit immediately after terminating the perpendicular current. The detection circuit collects a signal once a domain-wall pair passes through a coil.

The operation processes of the device are as follows. For both forward and reverse cycles, six repeated operations are implemented sequentially. In each cycle, the perpendicular current (J_1) is first used and then the in-plane current (J_2) is used [Figs. 6(b) and 6(e)]. Fig. 6(d) addresses the forward process. After nucleation, a meron is pushed to move rightward and later converted into a domain-wall pair at the interface between the wide and narrow tracks.[15] When the domain-wall pair goes through the region beneath the coil, the coil senses a varying magnetic flux and produces an

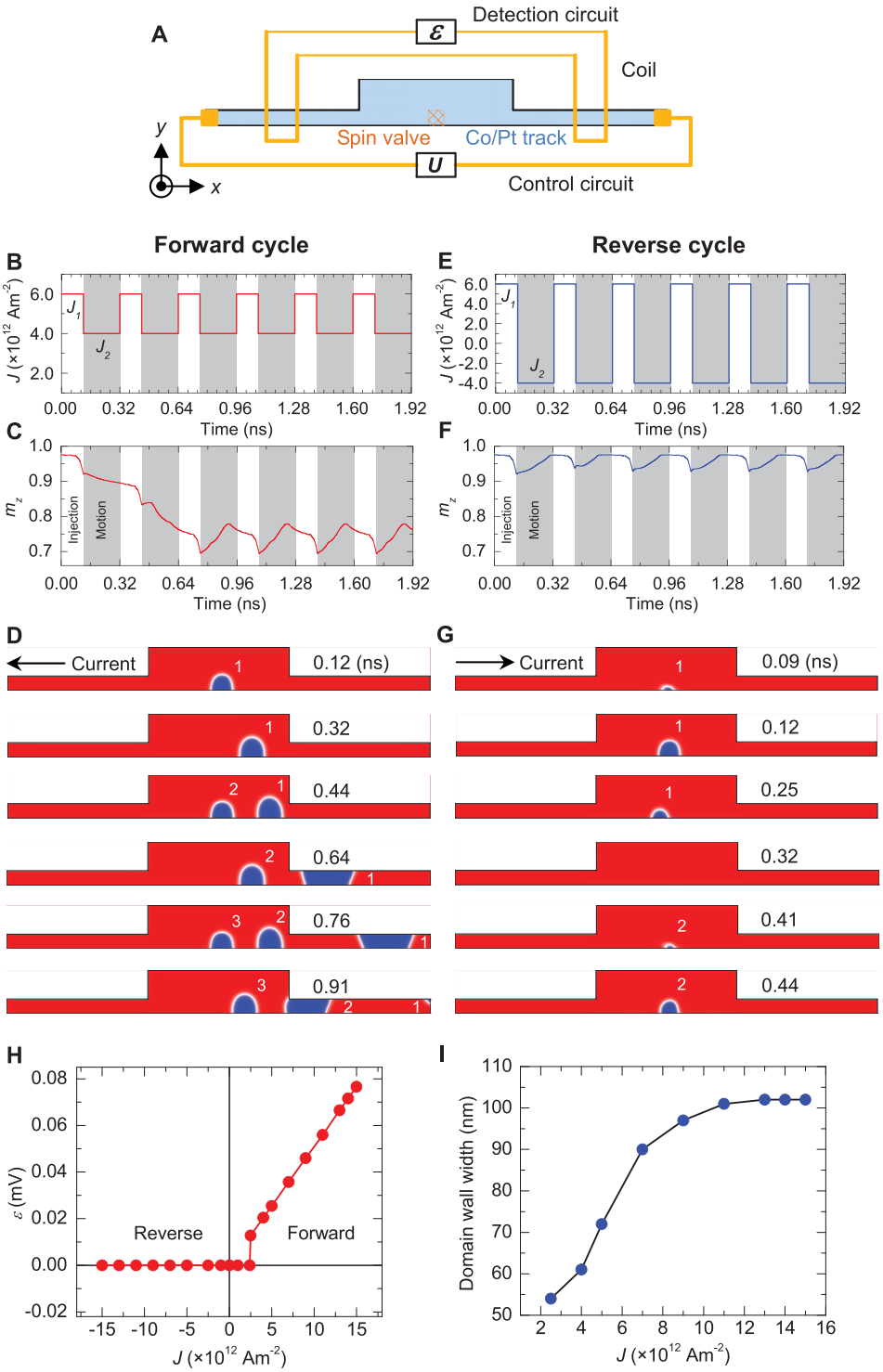

FIG. 6. Demonstration of a meron device. (a) Schematic architecture of the device. The lateral junction made of a width-modulated nanotrack is the functional element, where the unidirectional motion of merons is realized. The "carriers"—merons—are injected into the junction by a vertical current across a point-contact spin valve situated near the lower boundary. The junction is "biased" by an in-plane current supplied by the control circuit; once created, a meron goes into one of the two motional modes, depending on the current direction. The detection circuit outputs a signal by recording the magnetic-flux variation across the coils attached atop the narrow arms of the junction. Note that, here, the out-of-plane and in-plane current densities are denoted as J_1 and J_2, respectively. (b)–(d) The forward and (e)–(g) reverse operations on the device. Each instance contains 6 operation cycles. (b) and (e) Current sequences used to inject and manipulate the edge-merons. (c) and (f) Evolution of m_z with the operational time. (d) and (g) Carrier distribution inside the junction at characteristic times. (h) "I–V" (here, ε–J indeed) curve of the meron device. Here, ε is the induced electromotive force in the coils. (i) Domain-wall width as a function of in-plane current density J for the forward cycle. The domain-wall pair is converted from the meron at the connection area between the wide and narrow arms. Here, $w_b = 3w_n = 60$ nm and $l_b = l_n = 200$ nm.

electromotive force. Finally, the domain-wall pair leaves the junction from the right terminal. More than one meron can proceed in the junction simultaneously; there will be no coupling between any two of the merons and domain-wall pairs[8] if the temporal profile of the current sequence is well designed. The duration of J_1 cannot be too short in order for a meron to be formed [the injection processes of an edge-meron are illustrated in Fig. S3 for several sets of (K_u, D, α)]. J_2 should be sufficiently long to prevent clogging of merons in the track.[15] As shown in Fig. 6(c), the vertical magnetization decreases with the increase in the number of merons injected into the junction. At 0.80 ns, the domain-wall pair touches the right end of the junction, and the vertical magnetization begins to rise. The periodic oscillation of magnetization features the reproducible manipulation of merons by the repeated current pulses. As indicated in Fig. 6(g), for the reverse process, only a single meron is present in the junction at a given time, because the former meron has been dissolved during the action of each J_2 not until the initiation of the next J_1. In this case, the merons are annihilated in the central track and cannot enter the narrow arms to contribute an electromotive voltage.

Quantifying the forward and reverse processes, one can acquire the characteristic curve of the meron device as shown in Fig. 6(h) (equivalent to the "*I*–*V*" curve of a PN-junction diode[21]). The output of the device is encoded as the electromotive force, ε, induced in the coils of the detection circuit. After some calculation, one can arrive at $\varepsilon \equiv -d\Phi/dt = 2\mu_0 M_s \cdot w_n \cdot v_{dw}$, where Φ is the total magnetic flux across the coils (here, we assume a tiny spacing between the coil and junction planes and $\mathbf{B} = B\hat{e}_z$, where $B \approx \mu_0 H_z^d \approx \mu_0 M_s$ with $\mathbf{B}$ and H_z^d being the magnetic induction and the vertical component of the stray field at a point of the coil plane, respectively, from the narrow track), w_n the width of the narrow arms, and v_{dw} the domain-wall velocity in the narrow arm. Deriving $v_{dw}(J)$ from micromagnetic simulations and substituting it into the above expression, the $\varepsilon(J)$ is identified. On the reverse side, since the merons cannot reach the coils, the output is always zero. On the forward side, there exists a threshold current density (J_{c1}), below which the meron cannot be sent into the narrow arm resulting in an output of zero. In fact, there is another threshold current density (J_{c2}, corresponding to the smallest periphery of a ring in Fig. 3) below which the steady-state meron motion is not permitted. However, the J_{c2} is smaller than J_{c1} and thus unable to manifest itself in the ε–J curve. Above J_{c1}, the output, ε, is directly proportional to the driving current density, J, because $\varepsilon \propto v_{dw}$ and in turn $v_{dw} \propto J$ [as is known from simulations and Eq. (2)]. The driving current cannot be too large; otherwise, excessive spin textures will nucleate at the ends of the junction[49] and move against the electric current, which will disrupt the regular operation of the device. Moreover, a high current should cause strong chaoticity in the spin dynamics[49,50] and even damage the sample by Joule heating. Finite-temperature micromagnetic simulations reveal that the device can work at room temperature (Fig. S4). Overheating of the junction because of Joule heating can be avoided, as the current pulses in each operation cycle are sufficiently short (320 ps in the demonstrated case). In real devices, the interval between cycles should be optimized to allow efficient thermal dissipation.

As noticed from simulations, the domain-wall pair gets wider as the current density increases (Fig. 6(i)). The explanation is as follows. The width of the domain-wall pair is determined by the domain-wall velocity in the narrow track and the time required for a meron to be converted into a domain-wall pair. Both the domain-wall velocity and the conversion time are functions of the current density.

In Figs. 6(b) and 6(e), the current J_2 is pulsed and applied after J_1. In fact, our simulations demonstrate that J_2 can be utilized continuously (as a direct current) and only J_1 needs to be pulsed to periodically inject merons. Of course, using a direct current is not a good choice from the point of view of heat dissipation.

The driving current, J, in the junction comes from an external voltage, U, supplied by the control circuit. Substituting $U(J)$ into $\varepsilon(J)$, one finds that $\varepsilon/U = (\gamma\hbar/e)(\beta/\alpha) P \cdot \sigma \cdot [1/(l_b/w_b + l_n/w_n)]$, where σ is the conductivity of the junction material, and l_b (l_n) and w_b (w_n) are the length and width of the wide (narrow) track in the junction, respectively. This means that the ratio of the output to input voltages is independent of the current density and instead determined by the geometric (l_b, w_b, l_n, and w_n) and material (β, α, P, and σ) parameters of the junction. As such, materials with higher β/α[51,52] will bring enhanced output signals at a given current density, or a lowered effective range of current densities for a given magnitude of the output signal [as $\varepsilon \propto v_{dw} \propto (\beta/\alpha)J$]. It should be emphasized that the operation process of the device depends heavily on J, the driving current density.

For $\alpha = \beta$, the forward and reverse motions of a meron are equivalent, that is, no nonreciprocity happens to the meron motion. Because the Magnus force is absent, a meron moves along the electron current and meanwhile it decays under the outward directed drag force from the boundary. Consequently, the device cannot work at $\alpha = \beta$.

To prevent a meron from entering the left arm, the central track should be made longer than the propagation distance (tens to hundreds of nanometers; see Fig. S2) from the injection site to the annihilation site of an edge-meron.

IV. DISCUSSION

The Thiele equation, Eq. (1), neglects the mass of the moving merons and thus can only approximately uncover the real dynamics of the current-driven merons, which causes a slight quantitative discrepancy between the theoretical prediction and the simulation results. However, the key prediction of the Thiele equation—the unidirectional motion of edge-merons—is confirmed by micromagnetic simulations. Therefore, the massless Thiele equation[8,10,19,20] captures the core of the meron-motion dynamics in this system. The generalized Thiele equation[53,54] considering the mass of merons can be developed to improve our understanding on the meron dynamics, which is however beyond the scope of the present paper.

Recently, reliable conversion between a skyrmion and a domain-wall pair has been demonstrated,[15,55] and multiple interaction schemes between domain walls/skyrmions and spin waves have been identified.[24,27,41,48,56–60] Besides the well-known fact that domain walls are capable of modulating the propagation characteristics of spin waves,[56,57] it was demonstrated most recently that a magnetic nanotrack with imprinted domain-wall lines can serve as a graded-index "optic fiber" for channeling spin waves.[24,27,41] On the contrary, propagating spin waves can trigger domain-wall/skyrmion motion via a magnonic spin-transfer torque.[59,60] These findings have enriched the family of magnetic logic and memory devices.[15,22,23,27,56,61,62] The device presented here is built on a planar, track-based structure, which has been adopted in both domain-wall/skyrmion logic and racetrack memory devices,[15,22,23,27,56] and, remarkably, has also been employed in the mainstream magnonic logic devices based on propagating spin waves.[61,62] These facts imply that the meron device can be directly integrated into the existing logic and memory circuits as a signal controller, and furthermore, it can be conveniently reconfigured to perform other functions[8,15,27,41] as a reprogrammable device. Thus, the magnetic meron device as a new member of the diode family[24,63–68] is anticipated to play a crucial role in information

processing and data storage that are based on the magnetic features—skyrmions, domain-walls, and even spin waves.

It is worth noting that in the proof-of-principle demonstration of the proposed device, we use the Zhang-Li spin torque to drive edge-merons, and practically, the device performance can be greatly enhanced by optimizing the used materials, device geometry, and driving schemes. Alternatively, the emergent spin-orbit torques (spin Hall torque and/or Rashba torque) should be adopted to move the edge-merons in real devices, because these torques might allow the device to work at greatly reduced current densities, and additionally the restriction $\beta \neq \alpha$ required for device operation with the Zhang-Li torque can be released. In fact, most recently, Jiang *et al.*[69] have experimentally observed the skyrmion Hall effect, for which the current-induced spin Hall torque was used to drive skyrmions motion. This experiment gives a strong hint that the proposed device should function practically and the spin-Hall torque will be a more efficient means for operating the meron device.

SUPPLEMENTARY MATERIAL

See supplementary material for Figures S1−S4 that provide details on the current-dependent motion of edge-merons, the material-parameters dependence of the injection and unidirectional motion of edge-merons, and the diode effect at finite temperature. Figure S5 shows edge-meron motion in a nanotrack of B20-type materials with bulk Dzyaloshinskii-Moriya interaction.

ACKNOWLEDGMENTS

Y.Z. acknowledges the support by National Natural Science Foundation of China (Project No. 1157040329), the Seed Funding Program for Basic Research and Seed Funding Program for Applied Research from the HKU, ITF Tier 3 funding (ITS/203/14), the RGC-GRF under Grant HKU 17210014, and University Grants Committee of Hong Kong (Contract No. AoE/P-04/08). X.J.X. acknowledges the support by the National Natural Science Foundation of China under Grant No. 11104206.

[1]S. Mühlbauer, B. Binz, F. Jonietz, C. Pfleiderer, A. Rosch, A. Neubauer, R. Georgii, and P. Böni, Science **323**, 915 (2009).
[2]X. Z. Yu, Y. Onose, N. Kanazawa, J. H. Park, J. H. Han, Y. Matsui, N. Nagaosa, and Y. Tokura, Nature **465**, 901 (2010).
[3]S. Heinze, K. von Bergmann, M. Menzel, J. Brede, A. Kubetzka, R. Wiesendanger, G. Bihlmayer, and S. Blugel, Nat. Phys. **7**, 713 (2011).
[4]I. Dzyaloshinskii, J. Phys. Chem. Solids **4**, 241 (1958).
[5]T. Moriya, Phys. Rev. **120**, 91 (1960).
[6]A. Fert and P. M. Levy, Phys. Rev. Lett. **44**, 1538 (1980).
[7]A. Fert, Mater. Sci. Forum **59**, 439 (1990).
[8]J. Sampaio, V. Cros, S. Rohart, A. Thiaville, and A. Fert, Nat. Nanotechnol. **8**, 839 (2013).
[9]J. Iwasaki, M. Mochizuki, and N. Nagaosa, Nat. Nanotechnol. **8**, 742 (2013).
[10]J. Iwasaki, M. Mochizuki, and N. Nagaosa, Nat. Commun. **4**, 1463 (2013).
[11]J. Zang, M. Mostovoy, J. H. Han, and N. Nagaosa, Phys. Rev. Lett. **107**, 136804 (2011).
[12]L. Kong and J. Zang, Phys. Rev. Lett. **111**, 067203 (2013).
[13]X. Zhang, Y. Zhou, and M. Ezawa, Nat. Commun. **7**, 10293 (2016).
[14]M. Pereiro, D. Yudin, J. Chico, C. Etz, O. Eriksson, and A. Bergman, Nat. Commun. **5**, 4815 (2015).
[15]Y. Zhou and M. Ezawa, Nat. Commun. **5**, 4652 (2014).
[16]R. Rajaraman, *Solitons and Instantons: An Introduction to Solitons and Instantons in Quantum Field Theory* (North-Holland, Amsterdam, 1987), Vol. 15.
[17]A. A. Thiele, Phys. Rev. Lett. **30**, 230 (1973).
[18]X. Z. Yu, N. Kanazawa, W. Z. Zhang, T. Nagai, T. Hara, K. Kimoto, Y. Matsui, Y. Onose, and Y. Tokura, Nat. Commun. **3**, 988 (2012).
[19]J. Iwasaki, W. Koshibae, and N. Nagaosa, Nano Lett. **14**, 4432 (2014).
[20]S.-Z. Lin, C. Reichhardt, C. D. Batista, and A. Saxena, Phys. Rev. B **87**, 214419 (2013).
[21]G. W. Neudeck, *The PN Junction Diode* (Addison-Wesley, Reading, MA, 1989).
[22]D. A. Allwood, G. Xiong, C. C. Faulkner, D. Atkinson, D. Petit, and R. P. Cowburn, Science **309**, 1688 (2005).
[23]S. S. P. Parkin, M. Hayashi, and L. Thomas, Science **320**, 190 (2008).
[24]J. Lan, W. Yu, R. Wu, and J. Xiao, Phys. Rev. X **5**, 041049 (2015).
[25]H. Dery, P. Dalal, L. Cywinski, and L. J. Sham, Nature **447**, 573 (2007).
[26]Y. Zhou, E. Iacocca, A. A. Awad, R. K. Dumas, F. C. Zhang, H. B. Braun, and J. Åkerman, Nat. Commun. **6**, 8193 (2015).
[27]X. Xing and Y. Zhou, NPG Asia Mater. **8**, e246 (2016).
[28]S. Zhang and Z. Li, Phys. Rev. Lett. **93**, 127204 (2004).
[29]A. Thiaville, Y. Nakatani, J. Miltat, and Y. Suzuki, Europhys. Lett. **69**, 990 (2005).
[30]A. Pushp, T. Phung, C. Rettner, B. P. Hughes, S.-H. Yang, L. Thomas, and S. S. P. Parkin, Nat. Phys. **9**, 505 (2013).
[31]Y. Nakatani, A. Thiaville, and J. Miltat, Nat. Mater. **2**, 521 (2003).
[32]V. E. Demidov, J. Jersch, S. O. Demokritov, K. Rott, P. Krzysteczko, and G. Reiss, Phys. Rev. B **79**, 054417 (2009).
[33]A. Vansteenkiste, J. Leliaert, M. Dvornik, M. Helsen, F. Garcia-Sanchez, and B. van Waeyenberge, AIP Adv. **4**, 107133 (2014).
[34]A. Thiaville, S. Rohart, E. Jué, V. Cros, and A. Fert, Europhys. Lett. **100**, 57002 (2012).
[35]L. D. Landau and E. M. Lifshitz, Phys. Z. Sowjetunion **8**, 153 (1935).
[36]T. L. Gilbert, IEEE Trans. Magn. **40**, 3443 (2004).
[37]J. Slonczewski, J. Magn. Magn. Mater. **159**, L1–L7 (1996).
[38]N. Fujita, N. Inaba, F. Kirino, S. Igarashi, K. Koike, and H. Kato, J. Magn. Magn. Mater. **320**, 3019 (2008).
[39]R. Tomasello, E. Martinez, R. Zivieri, L. Torres, M. Carpentieri, and G. Finocchio, Sci. Rep. **4**, 6784 (2014).
[40]J. M. Shaw, H. T. Nembach, and T. J. Silva, Appl. Phys. Lett. **105**, 062406 (2014).
[41]F. Garcia-Sanchez, P. Borys, R. Soucaille, J.-P. Adam, R. L. Stamps, and J.-V. Kim, Phys. Rev. Lett. **114**, 247206 (2015).
[42]X. Zhang, G. P. Zhao, H. Fangohr, J. P. Liu, W. X. Xia, J. Xia, and F. J. Morvan, Sci. Rep. **5**, 7643 (2015).
[43]V. E. Demidov, S. O. Demokritov, K. Rott, P. Krzysteczko, and G. Reiss, Appl. Phys. Lett. **92**, 232503 (2008).
[44]X. Xing, S. Li, X. Huang, and Z. Wang, AIP Adv. **3**, 032144 (2013).
[45]J. Jorzick, S. O. Demokritov, B. Hillebrands, D. Berkov, N. L. Gorn, K. Guslienko, and A. N. Slavin, Phys. Rev. Lett. **88**, 047204 (2002).
[46]J. P. Park, P. Eames, D. M. Engebretson, J. Berezovsky, and P. A. Crowell, Phys. Rev. Lett. **89**, 277201 (2002).
[47]S. O. Demokritov and V. E. Demidov, in *Spin Wave Confinement*, edited by S. O. Demokritov (Pan Stanford Publishing Pte. Ltd., Singapore, 2009), Chap. 1.
[48]F. Ma, Y. Zhou, H. B. Braun, and W. S. Lew, Nano Lett. **15**, 4029 (2015).
[49]P. Sethi, C. Murapaka, G. J. Lim, and W. S. Lew, Appl. Phys. Lett. **107**, 192401 (2015).
[50]S. M. Seo, K. J. Lee, H. Yang, and T. Ono, Phys. Rev. Lett. **102**, 147202 (2009).
[51]M. Eltschka, M. Wötzel, J. Rhensius, S. Krzyk, U. Nowak, M. Kläui, T. Kasama, R. E. Dunin-Borkowski, L. J. Heyderman, H. J. van Driel, and R. A. Duine, Phys. Rev. Lett. **105**, 056601 (2010).
[52]O. Boulle, J. Kimling, P. Warnicke, M. Kläui, U. Rüdiger, G. Malinowski, H. J. M. Swagten, B. Koopmans, C. Ulysse, and G. Faini, Phys. Rev. Lett. **101**, 216601 (2008).
[53]O. A. Tretiakov, D. Clarke, G.-W. Chern, Ya. B. Bazaliy, and O. Tchernyshyov, Phys. Rev. Lett. **100**, 127204 (2008).
[54]I. Makhfudz, B. Krüger, and O. Tchernyshyov, Phys. Rev. Lett. **109**, 217201 (2012).
[55]W. Jiang, P. Upadhyaya, W. Zhang, G. Yu, M. B. Jungfleisch, F. Y. Fradin, J. E. Pearson, Y. Tserkovnyak, K. L. Wang, O. Heinonen, S. G. E. te Velthuis, and A. Hoffmann, Science **349**, 283 (2015).
[56]R. Hertel, W. Wulfekel, and J. Kirschner, Phys. Rev. Lett. **93**, 257202 (2004).

[57]J. Iwasaki, A. J. Beekman, and N. Nagaosa, Phys. Rev. B **89**, 064412 (2014).
[58]S. J. Hermsdoerfer, H. Schultheiss, C. Rausch, S. Schafer, B. Leven, S.-K. Kim, and B. Hillebrands, Appl. Phys. Lett. **94**, 223510 (2009).
[59]D.-S. Han, S.-K. Kim, J.-Y. Lee, S. J. Hermsdoerfer, H. Schultheiss, B. Leven, and B. Hillebrands, Appl. Phys. Lett. **94**, 112502 (2009).
[60]P. Yan, X. S. Wang, and X. R. Wang, Phys. Rev. Lett. **107**, 177207 (2011).
[61]M. P. Kostylev, A. A. Serga, T. Schneider, B. Leven, and B. Hillebrands, Appl. Phys. Lett. **87**, 153501 (2005).
[62]A. V. Chumak, A. A. Serga, and B. Hillebrands, Nat. Commun. **5**, 4700 (2014).
[63]B. Li, L. Wang, and G. Casati, Phys. Rev. Lett. **93**, 184301 (2004).
[64]C. W. Chang, D. Okawa, A. Majumdar, and A. Zettl, Science **314**, 1121 (2006).
[65]B. Liang, X. S. Guo, J. Tu, D. Zhang, and J. C. Cheng, Nat. Mater. **9**, 989 (2010).
[66]D.-W. Wang, H.-T. Zhou, M.-J. Guo, J.-X. Zhang, J. Evers, and S.-Y. Zhu, Phys. Rev. Lett. **110**, 093901 (2013).
[67]S. Borlenghi, W. Wang, H. Fangohr, L. Bergqvist, and A. Delin, Phys. Rev. Lett. **112**, 047203 (2014).
[68]A. A. Tulapurkar, Y. Suzuki, A. Fukushima, H. Kubota, H. Maehara, K. Tsunekawa, D. D. Djayaprawira, N. Watanabe, and S. Yuasa, Nature **438**, 339 (2005).
[69]W. Jiang, X. Zhang, G. Yu, W. Zhang, X. Wang, M. B. Jungfleisch, J. E. Pearson, X. Cheng, O. Heinonen, K. L. Wang, Y. Zhou, A. Hoffmann, and S. G. E. te Velthuis, "Direct observation of the skyrmion Hall effect," Nat. Phys. (published online).